THE ASTROPHYSICAL JOURNAL, 375:652–662, 1991 July 10

SIX BALMER-DOMINATED SUPERNOVA REMNANTS[1]

R. CHRIS SMITH[2] AND ROBERT P. KIRSHNER[2,3]
Harvard-Smithsonian Center for Astrophysics, 60 Garden Street, Cambridge, MA 02138
WILLIAM P. BLAIR[2,3]
Center for Astrophysical Sciences, The Johns Hopkins University, Baltimore, MD 21218
AND
P. FRANK WINKLER[3]
Middlebury College, Department of Physics, Middlebury, VT 05753
Received 1990 October 19; accepted 1991 January 10

ABSTRACT

We present optical spectra of six Balmer-dominated supernova remnants (SNRs): the Galactic remnants of SN 1572 (Tycho) and SN 1006, and four remnants in the Large Magellanic Cloud (LMC), 0505−67.9, 0509−67.5, 0519−69.0, and 0548−70.4. All except 0509−67.5 exhibit broad (580–2300 km s^{-1} FWHM) Hα emission characteristic of collisionless shocks. We have measured the line widths and compared them to models for a collisionless shock interacting with a partially neutral medium. From this comparison, we derive a shock velocity for each remnant with broad Hα and a possible lower limit to the shock velocity in 0509−67.5. Although previous analyses used the ratio of broad to narrow intensity as an indicator of shock velocity, our models show that this is not reliable. Further, the observed intensity ratios do not correspond to either the commonly assumed case of no equilibration ($T_e \ll T_{ion}$), or to the other extreme of total equilibration ($T_e = T_{ion}$).

By combining the observed proper motions of filaments in Tycho and SN 1006 with our estimates of the shock velocities, we obtain distances to these remnants of 1.5–3.1 kpc and 1.4–2.8 kpc, respectively. The shock velocities derived for the LMC remnants allow us to estimate their ages. The ages range from $\sim 10^4$ yr for the two which show evidence of transition to radiative shocks, 0505−67.9 and 0548−70.4, to less than 1500 yr for the small remnants 0509−67.5 and 0519−69.0. These two young remnants bring the number of supernovae in the LMC to at least five in the past 1500 yr, making the supernova rate per unit luminosity comparable to that reported for late spiral galaxies.

Subject headings: nebulae: internal motions — nebulae: supernova remnants — shock waves

1. INTRODUCTION

The optical spectrum of a typical supernova remnant (SNR) exhibits forbidden emission lines of oxygen, nitrogen, and sulfur, as well as the hydrogen Balmer series (Fesen, Blair, & Kirshner 1985). The wide range of ionization, the correlation of electron temperature with ionization, and the abundances derived from the observed line strengths all indicate that these lines come from shocked interstellar material that is cooling radiatively (as modeled, for example, by Raymond 1979 or Dopita 1977). In contrast, a few remnants display strong Balmer lines with little or no evidence of the forbidden lines seen in radiative shock spectra.

The nature of these Balmer-dominated shocks was explained by Chevalier & Raymond (1978, hereafter CR), who proposed that the spectrum was due to a collisionless shock moving into partially neutral interstellar material. They predicted a Balmer line profile consisting of a narrow component, from collisionally excited neutrals behind the shock, and a broad component due to charge exchange. Such a line profile was detected by Chevalier, Kirshner, & Raymond (1980, hereafter CKR) in the remnant of SN 1572 (Tycho). These shocks are also referred to as nonradiative shocks (McKee & Hollenbach 1980), since radiation does not significantly affect the dynamics behind the shock.

Several instances of such shocks have since been found. The remnant of SN 1006, known to have a Balmer-dominated spectrum, was shown to exhibit the characteristic line profile by Kirshner, Winkler, & Chevalier (1987, hereafter KWC). Balmer-dominated shocks have also been found in the peripheries of some SNRs composed mostly of radiative shocks (e.g., the Cygnus Loop [Raymond et al. 1983] and RCW86 [Long & Blair 1990]) and in knotty and diffuse emission in Kepler's SNR (Fesen et al. 1989; Blair, Long, & Vancura 1991). In extragalactic systems, optical discovery of Balmer-dominated SNRs is unlikely since the searches select remnants based on large [S II] to Hα ratios (e.g., Long et al. 1990). X-ray surveys avoid this bias since they detect the hot shocked gas itself. From narrow-band imaging of remnants identified in the X-ray survey of the Large Magellanic Cloud (LMC) by Long, Helfand, & Grabelsky (1981) (see Mathewson et al. 1983), Tuohy et al. (1982) identified four SNRs which showed strong hydrogen emission and weak forbidden line emission. We present spectra of all four remnants, two of which have no previously published spectra.

[1] Based partly on observations obtained at the Multiple Mirror Telescope Observatory, a joint facility of the Smithsonian Astrophysical Observatory and the University of Arizona.

[2] Visiting Astronomer, Kitt Peak National Observatory, National Optical Astronomy Observatories, which is operated by Associated Universities for Research in Astronomy, Inc. (AURA) under cooperative agreement with the National Science Foundation.

[3] Visiting Astronomer, Cerro Tololo Inter-American Observatory, National Optical Astronomy Observatories.

The distinctive two-component line profile can be used to probe the kinematics of this type of shock. CKR showed how the shock velocity is related to the width of the broad component and independently estimated the shock velocity from the ratio of the intensity in the broad component to that in the narrow component. In this work, we show that using the intensity ratio is much more complicated than was previously thought, both on observational and theoretical grounds.

In this paper, we examine spectra of six Balmer-dominated SNRs: the Galactic remnants of SN 1572 (Tycho) and SN 1006, and the LMC remnants 0505−67.9, 0509−67.5, 0519−69.0, and 0548−70.4. In § 2, we describe the observations and fits to the Hα profiles which show evidence for a broad component. We calculate the widths of the broad components and the intensity ratios predicted by the CKR model (§ 3), and we use the widths to estimate shock velocities (§ 4). We combine these velocities with data in the literature to estimate distances, ages, and proper motions for these remnants.

2. OBSERVATIONS AND ANALYSIS

From the catalog of Mathewson et al. (1983), Tuohy et al. (1982) classified four remnants as Balmer-dominated based on narrow band Hα and [O III] λ5007 images, in which all four remnants showed strong Hα emission but little or no [O III]. Their spectra of the two smallest remnants showed only hydrogen emission, and one, 0519−69.0, showed a broad component in the Hα line. Here we present spectra for all four of these SNRs at a higher spectral resolution than Tuohy et al. (1982) with spatial information retained. In addition, we present a new long-slit spectrum for Tycho and reanalyze the KWC spectrum of SN 1006. The details of all of the observations are summarized in Tables 1A and 1B. All data were reduced using standard IRAF longslit procedures, and the resulting spectra are shown in Figures 2, 3, 5, and 6.

Where broad components were detected (or suspected) in our spectra, line strengths, widths, and centers were determined by fitting two Gaussians to the Hα profile with a χ^2 minimization routine. In all cases, the width of the narrow component was consistent with the width of the night sky lines. The uncertainties quoted are at approximately 1 σ levels. Table 2 lists the resulting best-fit broad FWHM and broad-to-narrow intensity ratio, I_b/I_n, for each of the six SNRs.

2.1. *Galactic Balmer-dominated Remnants*

2.1.1. *Tycho (SN 1572)*

Tycho is the prototypical Balmer-dominated SNR. Minkowski (1959) first noted that the remnant was visible only in hydrogen emission. A spectrum by Kirshner & Chevalier (1978) showed no evidence of any lines other than Balmer lines down to 10% of Hα. CKR discovered the broad component to Hα predicted by CR, and more recently, KWC derived a FWHM of 1800 ± 100 km s^{-1} and an intensity ratio of $I_b/I_n = 1.08 \pm 0.16$.

Our spectrum was obtained with the "Red Channel" longslit spectrograph (Schmidt, Weymann, & Foltz 1989) on the Multiple Mirror Telescope (MMT, see Table 1A), providing both spatial and spectral information. The slit was placed with a position angle of −10° at the position of Kamper & van den Bergh's (1978) knot "g" taking into account the observed proper motion. This slit position includes the knot and the adjacent filament extending to the south. Knot g and the slit are shown in Figure 1, an image of Tycho in Hα taken on the KPNO 4 m telescope on 1990 September 28. The MMT spectrum shows a strong broad component, with no evidence of

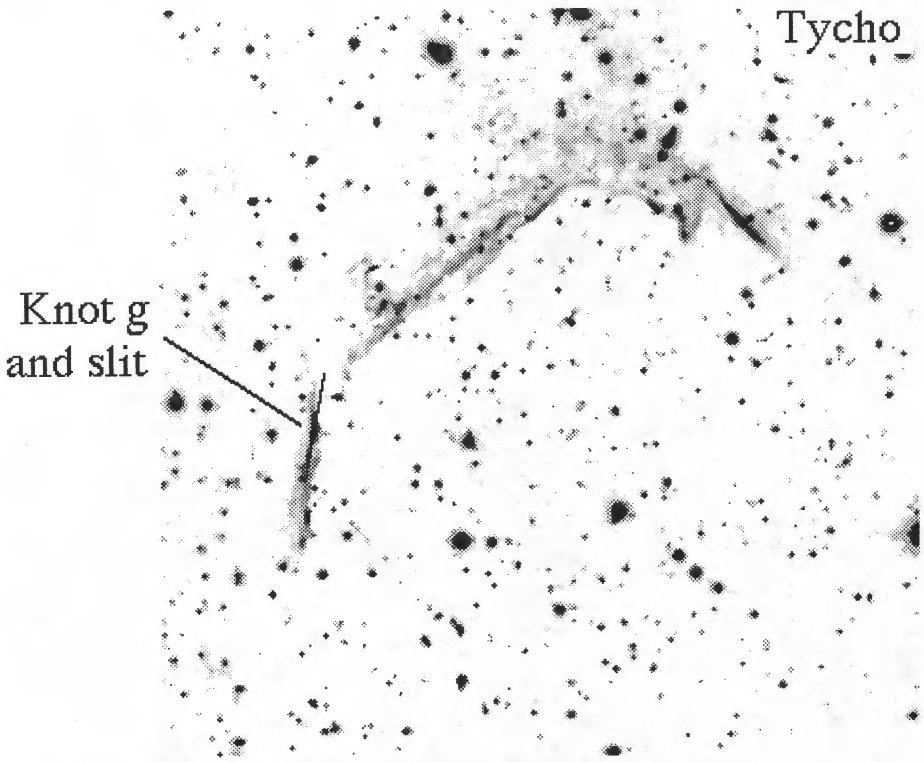

FIG. 1.—Slit position for observations of Tycho's SNR. (North is up, and east is to the left.)

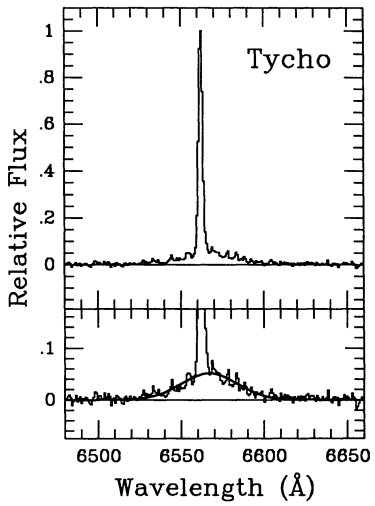

FIG. 2.—Hα line profile from knot "g" in Tycho. Upper panel shows relative intensities of narrow and broad components, and lower panel shows the best fit to broad component.

any lines other than Hα in the wavelength interval 6345–6950 Å down to 5% the strength of the narrow Hα component. Typical radiative shocks have [N II] λλ6548, 6583 lines with strength 25%–50% of Hα and [S II] λλ6717, 6731 lines with strength 40%–100% of Hα (Fesen, Blair, & Kirshner 1985).

The line profiles in spectra extracted from different places along the slit vary significantly, from a strong broad component in the knot to little or no broad component in the noisy spectrum of the southern filament. Averaging over the knot alone, we obtained a FWHM of 1900 ± 300 km s^{-1} (the large uncertainty results from variation in FWHM depending on position). This FWHM represents an average over the shock velocities in the knot, weighted by brightness. Since the proper motion of the knot is measured based upon the brightest portions, this "average" shock velocity should correspond to the measured proper motion of the bright knot. The best fit to the broad component is shown in Figure 2. The measured intensity ratio, I_b/I_n, is 0.77 ± 0.09, significantly lower than the KWC value of 1.08 ± 0.16. However, due to the variation with position, different aperture positions yield different results. The center of the broad component is shifted 5 ± 1 Å, or 240 ± 60 km s^{-1}, to the red with respect to that of the narrow component, in agreement with the observation of KWC.

2.1.2. *SN 1006*

The spectrum of SN 1006 presented here is from KWC. We include it because improved fitting techniques allow the previous results to be refined. The observational setup is detailed in Tables 1A and 1B. The slit was positioned at a small angle across one of the brightest filaments in the NW rim of the remnant, and the spectrum was extracted by summing along this filament.

With this spectrum, KWC confirmed the existence of broad Hα emission in this remnant, measuring a FWHM of 2600 ± 100 km s^{-1} and an intensity ratio I_b/I_n of 0.77 ± 0.08. No lines other than Hα are seen in the spectrum. Our more quantitative line fitting algorithm gives a FWHM of 2310 ± 210 km s^{-1} for the broad component, with an intensity ratio of 0.73 ± 0.06. The data and the best-fit broad component are shown in Figure 3. No significant variation in the line profile was detected in spectra extracted from different locations along the filament.

2.2. *Balmer-dominated SNRs in the LMC*

Spectra of the four Balmer-dominated SNRs in the LMC were taken on two consecutive nights in 1984 November on the CTIO 4 m telescope. A 3″ by 200″ slit was used with the

TABLE 1A

OBSERVATIONS OF BALMER-DOMINATED SNRs

SNRs	UT Date	Telescope	Detector	Spectral Resolution (Å)
Tycho	1988 Oct 2	MMT	TI CCD	2.6
SN 1006	1986 Mar 4	CTIO 4 m	GEC CCD	3.6
LMC SNRs	1984 Nov 29, 30	CTIO 4 m	GEC CCD	2.1

TABLE 1B

SLIT POSITIONS AND INTEGRATION TIMES

SNR	Slit Position (1950 Coordinates) R.A.	Decl.	Offset from Center[a]	Position Angle	Total Integration Time (s)
Tycho	$00^h23^m06^s$	+63°52′40″	...	−10°	5400
SN 1006	14 59 03	−41 33 13	...	72	10800
0505−67.9	05 05 49	−67 56 33	5″ N	90	2700
0509−67.5	05 09 36	−67 34 51	7″ S	90	2700
0519−69.0 position 1	05 19 52	−69 05 03	2″ N	90	1800
0519−69.0 position 2	05 19 52	−69 05 07	2″ S	90	1500
0548−70.4 position 1	05 48 23	−70 25 26	7″ N	90	2700
0548−70.4 position 2	05 48 23	−70 25 37	18″ S	90	2700
0548−70.4 position 3	05 48 23	−70 26 02	18″ N	90	2700

[a] LMC remnant centers from Tuohy et al. 1982.

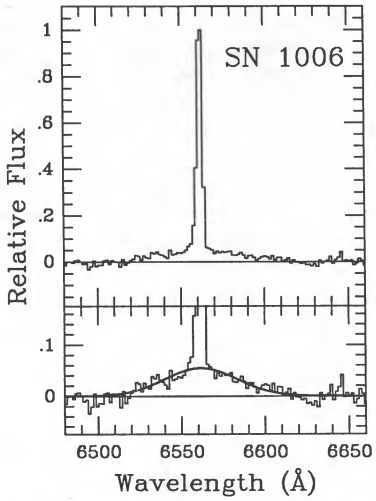

FIG. 3.—Hα line profile of SN 1006. Upper panel shows relative intensities of narrow and broad components, and lower panel shows the best fit to broad component.

R-C spectrograph, grating 450, and the red Air Schmidt camera with the GEC CCD, giving a spectral resolution of 2.1 Å and a spatial scale of 0.″6 pixel^{-1}. Slit positions, position angles, and exposures are given in Table 2. The images of 0509−67.5 and 0519−69.0 (Figs. 4*a* and 4*b*) are 1500 and 1000 s Hα exposures, respectively, obtained with the CTIO 4 m with the Prime Focus camera and the RCA1 CCD on 1988 February 16.

2.2.1. *0509−67.5*

Of the four remnants we studied in the LMC, 0509−67.5 has the most uniform shell structure in Hα. It is also the smallest, and probably the youngest (see discussion, § 4.3). Our slit position intercepts the bright southwestern and southeastern portions of the rim (see Fig. 4*a*). Tables 1A and 1B give the detailed description of the observational setup for the LMC SNRs. As shown in the spectrum (Fig. 5*a*), neither forbidden-line emission nor a broad Hα component was detected anywhere along the slit.

Using artificial spectra, made with broad components and intensity ratios typical of those observed in other remnants ($I_b/I_n \approx 0.7$–1.1), we ran tests to estimate the detection limits imposed by our data and fitting techniques. With the combination of resolution, wavelength coverage ($\lambda\lambda$6470–6900), and signal-to-noise ratio of our data, we found that we could detect broad components only up to about 1700 km s^{-1} FWHM for our LMC SNR data set. Thus, assuming that there is a broad component as seen in other remnants and as predicted by theory, we quote a lower limit of 1700 km s^{-1} for the FWHM. This is consistent with the line profile of Touhy et al. (1982), which also showed no broad component at a lower dispersion capable of detecting much broader emission.

2.2.2. *0519−69.0*

Observations of 0519−69.0 were made at two slit positions, listed in Table 1A, chosen to pass through the knot of strong Hα emission on the east rim and through the shell on the west side, as shown in the Hα image in Figure 4*b*. The resulting two-dimensional spectra show no forbidden-line emission down to about 5% of Hα, similar to the Galactic Balmer-dominated remnants and 0509−67.5. A detailed search of the spectra revealed only one location with broad Hα, in the east rim in slit position 1 (marked B on Fig. 4*b*). The spectrum at this location is shown in Figure 5*b*. Our fit to the Hα line gives a FWHM of 1300 ± 200 km s^{-1} and an intensity ratio of $I_b/I_n = 0.8 \pm 0.2$.

Tuohy et al. (1982) found significant broad emission with a 2800 ± 300 km s^{-1} FWHM in their low-dispersion spectrum

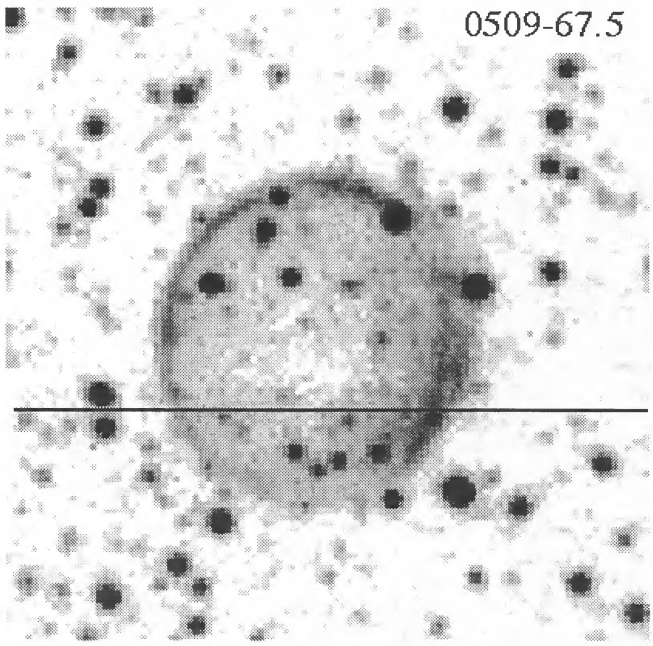

FIG. 4*a*

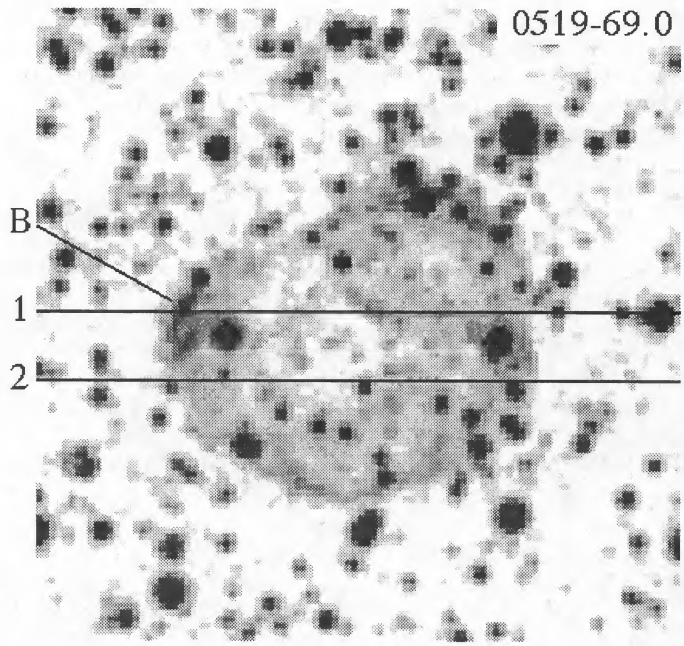

FIG. 4*b*

FIG. 4.—Hα images of (*a*) 0509−67.5 and (*b*) 0519−69.0, with slit positions marked. The location of detected broad component in 0519−69.0 is marked B. (North is up, and east is to the left in both figures.)

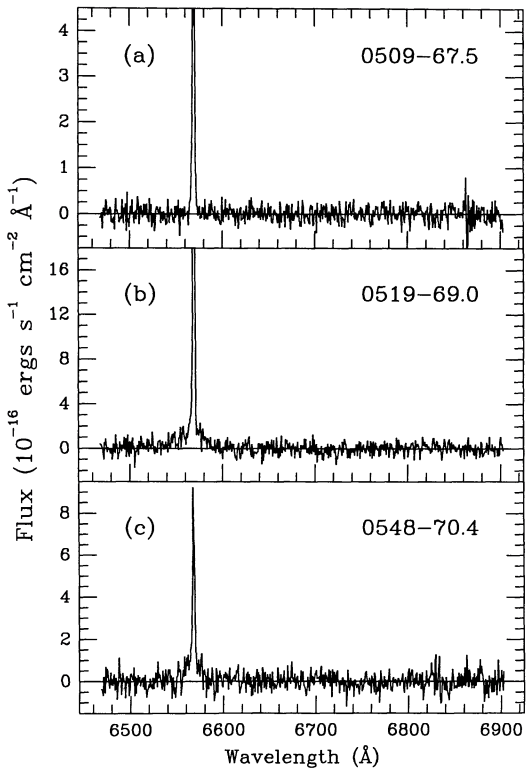

FIG. 5.—Spectra of (*a*) 0509 − 67.5, (*b*) 0519 − 69.0, and (*c*) 0548 − 65.7

of this remnant but did not detect any broad component in their high-dispersion spectrum. Although our results appear to contradict theirs, in reality they do not. We see a lower velocity-width broad line in only one location on the east rim, with no evidence of any broad component in the east rim at the second slit position, and no evidence of a broad component in either slit position on the west rim. Given the detection limitations for lines broader than 1700 km s^{-1} discussed in the previous section, the places where we see no broad line are consistent with Touhy et al.'s (1982) FWHM. The site of the narrower broad component may simply be a dense cloud where the shock is slower.

The absence of broad emission in most of the remnant presents a problem in interpreting the intensity ratio. Contamination by Hα from the regions with no detectable broad component decreases the observed intensity ratio I_b/I_n. Summing over different apertures along the eastern portion of slit position 1, the intensity ratios were found to vary from a high of 0.81 down to 0.5, with no significant variation in the best-fit FWHM. Since there may be significant emission too broad for us to detect, or narrow emission from a different mechanism, we quote a lower limit for the broad component: $I_b/I_n \gtrsim 0.7$.

2.2.3. *0548 − 70.4*

Spectra of 0548 − 70.4 were taken at the three slit positions listed in Table 1B. Slit positions 1 and 2 pass through the [O III] filaments noted by Tuohy et al. (1982), as well as both sides of the shell. Diffuse Hα emission is present throughout the remnant, with regions of pure Hα emission where the slits pass through the shell, and regions emitting [S II] and [N II] as well as Hα near the center of the slits, corresponding to [O III] filaments. Position 3 was chosen to pass through the Hα knot in the northwest of the remnant which is the brightest point in X-rays as shown by Mathewson et al. (1983). This position exhibits stronger forbidden-line emission, with some regions showing double peaked lines, with velocity separations of up to 170 km s^{-1}. The bright X-ray knot shows up as the brightest knot of Hα in the two-dimensional spectrum. The [S II]/Hα and [N II]/Hα line ratios in this knot, as well as all the other locations of radiative shocks in this remnant, are typical of the radiative shocks in other LMC SNRs.

Although all spectra of the rim of this remnant show only Hα emission, only the eastern rim in slit position 1 showed any indication of a broad component. The spectra of the two filaments crossing the slit at this position show weak broad emission with the same FWHM. To improve the signal, we added the two and refitted the line. The spectrum is shown in Figure 5*c*. The resulting fit gives a FWHM = 760 ± 140 km s^{-1} and an intensity ratio of $I_b/I_n = 1.1 \pm 0.2$.

2.2.4. *0505 − 67.9*

Tuohy et al. (1982) noted that, like 0548 − 70.4, 0505 − 67.9 showed strong Hα emission with only a few knots of faint [O III] emission. Our slit position for this remnant (Table 1B) was chosen to pass through the knots of emission in the northwest identified in Tuohy et al.'s (1982) [O III] image, as well as the east and west portions of the shell. The two-dimensional spectrum shows diffuse Hα emission throughout the remnant, with two distinct regions of forbidden-line emission in both east and west rims, corresponding to the filaments seen in Tuohy et al.'s (1982) Hα image. Hα emission without forbidden lines is seen between the filaments and extending ~2″ beyond the outer filament of each rim. On the eastern rim, the inner filament shows a blueshift of approximately 80 km s^{-1} relative to the outer filament (based on fits to the [S II] lines). The filaments on the west rim show a similar velocity difference, although it is more difficult to determine due to the width of the [S II] lines in the inner filament. Such a complicated morphology is most likely due to curvature of the shock front. Higher resolution images of this remnant would provide interesting information on this apparent mixture of radiative and nonradiative shocks.

Broad Hα is present in the rims of 0505 − 67.9; however, separating the emission of the nonradiative shocks from that of the radiative shocks proved to be impossible at our slit position. The broad component is strongest around the outer filament on each rim. Figure 6 illustrates this with a sequence of spectra progressing through the eastern rim from the outermost edge to the inner filament. The western rim exhibits a similar progression. The nitrogen lines [N II] λ6583 and λ6548 add to the problem of extracting the Hα profile, due to the blending of the [N II] lines with the broad component.

To obtain an estimate of the FWHM of the broad component in each rim, we extracted spectra from different locations in the rim, as in Figure 6. We first removed the [N II] lines in these spectra by subtracting two Gaussians at the proper wavelengths. The flux and line center of [N II] λ6583 were determined by fitting the line with a Gaussian of the same width as the unblended [S II] lines λλ6717 and 6731, to try to minimize the effect of blending with the broad component; the flux and line center of [N II] λ6548 were determined from the known line ratio, λ6548/λ6583 = ⅓, and separation of the [N II] lines. We then fitted the Hα profiles in the resulting spectra with two Gaussians and took a weighted mean of the

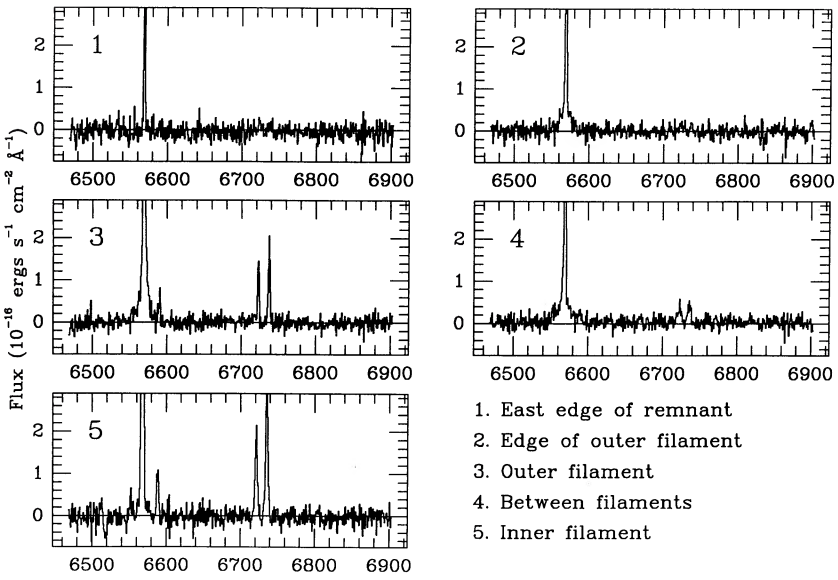

FIG. 6.—A series of spectra of 0505−67.9, taken from the east rim of the remnant. Note the changes in the broad component, and in the spectrum as a whole, as one moves through the filaments.

resulting best-fit FWHM and intensity ratios, weighting the spectra with high S/N and a strong broad component more heavily than others. We took the spread in the FWHM from all of the fits in each rim to be the uncertainty in the resulting FWHM for that rim. For the eastern rim, our best estimate of the FWHM is 600 ± 75 km s^{-1}, and for the western rim, our best estimate is FWHM $= 500 \pm 150$ km s^{-1}. The intensity ratios for these spectra are not really applicable to Balmer-dominated shocks, as they are contaminated by radiative shock emission. We include them only as lower limits for further discussion in the analysis of the shocks in this remnant. Our best estimate for the eastern rim is $I_b/I_n \gtrsim 0.6$, and for the western rim, $I_b/I_n \gtrsim 0.7$. Since the fits of Hα from both rims are consistent with a single line profile, we combined the results into best-fit parameters for this remnant of FWHM $= 580 \pm 70$ km s^{-1} and $I_b/I_n \gtrsim 0.7$.

The results of fitting the Hα line profiles are summarized in Table 2. Our detection of broad components in 0548−70.4 and 0505−67.9 brings the total number of remnants with filaments which show such a component up to eight, including the Cygnus Loop (Raymond et al. 1983), Kepler's SNR (Fesen et al. 1989; Blair, Long, & Vancura 1991), and RCW 86 (Long & Blair 1990). For these remnants, one can estimate the shock velocity from the width of the broad component, using calculations based on the CKR model described below. The confusion produced by narrow Hα emission near the region producing the two-component profile makes the intensity ratio difficult to measure. As discussed in the following section, this fact combined with the model sensitivity of the intensity ratio makes it a poor estimator of the shock velocity. However, the intensity ratio may be useful in determining other shock parameters.

TABLE 2

Hα LINE PROFILE PARAMETERS

SNR	FWHM of Broad Component (km s^{-1})	Intensity Ratio from Nonradiative Shock Component
Tycho	1900 ± 300	0.77 ± 0.09
SN 1006	2310 ± 210	0.73 ± 0.06
0505−67.9	580 ± 70	≥ 0.7
0509−67.5	...	...
0519−69.0	1300 ± 200	≥ 0.7
0548−70.4	760 ± 140	1.1 ± 0.2

3. THE MODEL

In the collisionless shock model proposed by CR and expanded in CKR, slow-moving neutral atoms in the preshock medium pass through the shock front largely unaffected. In the hot postshock medium, any of three processes may take place: ionization, excitation, or charge transfer. The dominant process in such a hot medium is ionization, but there is a finite probability that a neutral atom will be collisionally excited before being ionized. CR give the number of Hα photons produced per ionization as $\epsilon_A = 0.048$ for case A and $\epsilon_B = 0.27$ for case B, where case A refers to a medium which is optically thin to all H emission, and case B refers to a medium which is optically thick in the Lyman lines.

Collisional excitation of the slow neutral atoms results in narrow Hα emission, with a width determined by pre-shock conditions (e.g., the preshock temperature, although see Raymond et al. 1983). Charge exchange from slow neutrals to fast protons in the postshock medium produces broad Hα emission directly through exchange into excited states of the capturing proton. This reaction also gives fast neutrals which may be excited before being ionized, giving additional broad emission. Using the model described in CKR, we calculate the dependence of the width of the broad component on the shock velocity and also calculate the relation of the intensity ratio to shock velocity.

In all of the model calculations, we make use of a coordinate system in which the shock is moving with velocity v_s along the z-axis, perpendicular to our line of sight, which we set to be

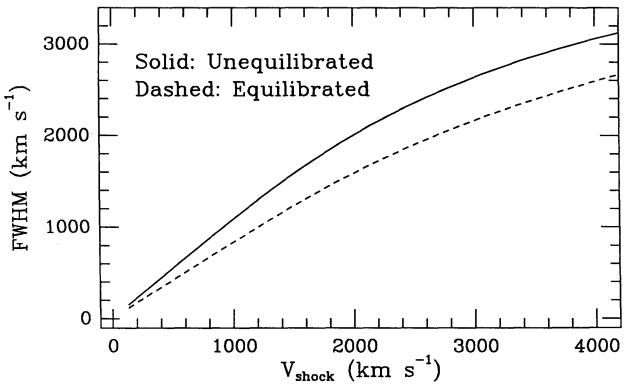

FIG. 7.—The calculated relations between FWHM of the broad component and the shock velocity. The curves represent the upper (unequilibrated) and lower (equilibrated) extremes for the FWHM at a given shock velocity. This is very similar to that calculated by CKR (Figure 3), though note that we use a different abscissa.

along the x-axis. The major uncertainty in these calculations is the manner in which energy is shared between ions and electrons. Coulomb equilibration is not rapid at energies and densities characteristic of nonradiative shocks, so one limit on the ion and electron temperatures is that of no equilibration, giving $T_{i,e} = 3m_{i,e}v_s^2/16k$, where $T_{i,e}$ and $m_{i,e}$ are the ion and electron temperatures and masses, respectively. The other extreme, complete equilibration with $T_e = T_i$, may result from plasma instabilities (McKee 1974; McKee & Hollenbach 1980). We calculate relations for both the broad-component FWHM versus shock velocity and intensity ratio versus shock velocity at both extremes of equilibration.

In the coordinate system described above, we can write the line profile of the broad component as in CKR,

$$\phi(v_x) \propto \int_{-\infty}^{+\infty} v\sigma_x(v)\{\exp[-l^2(v^2 - 2v_0 v_z)]\}dv_y\, dv_z\,, \qquad (1)$$

where $\sigma_x(v)$ is the cross section for charge transfer, $l^2 = m_i/2kT_i$, and v_0 is the bulk velocity of the postshock gas. For a strong adiabatic shock with $\gamma = 5/3$, $v_0 = \frac{3}{4}v_s$. In this equation it is assumed that ionization by neutral particles is negligible and that the probability of Hα emission is independent of proton velocity. For $\sigma_x(v)$, we used the analytic fit given by Freeman & Jones (1974). Figure 7 shows the calculated broad-component FWHM versus shock velocity for the equilibrated ($T_e = T_i$) and unequilibrated ($T_e \ll T_i$) extremes. This relation provides a clean-cut determination of the shock velocity from the observed broad FWHM, at least up to the uncertainty of equilibration, since the two curves represent the extremes of the FWHM (the only dependence on equilibration is in the T_i in l^2). The relation is not even particularly sensitive to the atomic physics used, as the relation calculated here differs little from that presented in CKR's Figure 3 (though note the differing abscissas), where they used a less accurate approximation to $\sigma_x(v)$ based on data from McClure (1966).

The calculated intensity ratio, however, *is* sensitive to the input physics and does not produce such an immediately useful relation. The ratio of intensities of the components can be obtained by estimating the fraction of fast neutrals versus the fraction of slow neutrals, given in CKR as

$$\frac{f_f}{f_s} = \frac{\langle\sigma_x v\rangle_s}{\langle\sigma_i v\rangle_f}\,, \qquad (2)$$

and adding terms to allow for charge exchange into excited states. Here $\langle\sigma_i v\rangle_f$ is the sum of the reaction rate coefficients for ionization by protons and electrons. The $\langle\ \rangle_s$ denotes an average over the velocity difference between the slow neutrals and the fast charged particles, and the $\langle\ \rangle_f$ represents an average over the velocity difference between the fast neutrals and the fast charged particles. The partially neutral preshock gas will be optically thin for the broad component emission (case A), but may be optically thick for Lyman emission in the narrow component (case B). Thus, the ratio of photons produced by excitation is $\epsilon_A f_f/\epsilon_B f_s$, where ϵ_A and ϵ_B are the appropriate Hα "efficiencies" from CR for the two cases. Since the Lyman emission may be only partially reprocessed, this may lead to an underestimate of the intensity ratio.

Following the discussion in CKR, one obtains an equation with three terms; the first collisional excitation, the second from charge exchange into excited states from slow neutrals, and the third from charge exchange into excited states from fast neutrals, so that the intensity ratio is given by

$$\frac{I_b}{I_n} = \frac{\epsilon_A f_f}{\epsilon_B f_s} + \frac{g_\alpha f_f}{\epsilon_B f_s} + \frac{g_\alpha f_f}{\epsilon_B f_s}\frac{\langle\sigma_x v\rangle_f}{\langle\sigma_i v\rangle_f}\,, \qquad (3)$$

or, somewhat simplified using equation (2),

$$\frac{I_b}{I_n} = \frac{\langle\sigma_x v\rangle_s}{\langle\sigma_i v\rangle_f}\left[\frac{\epsilon_A}{\epsilon_B} + \frac{g_\alpha}{\epsilon_B}\left(1 + \frac{\langle\sigma_x v\rangle_f}{\langle\sigma_i v\rangle_f}\right)\right]. \qquad (4)$$

This is the same relation used in CKR, though a typographical error in that paper caused the ϵ_B factor under g_α to be omitted. This error propagated into following papers, for example KWC Figure 5, where the incorrect relation is plotted.

The factor g_α is the fraction of charge transfers to excited states yielding Hα photons, either directly or following cascading, as calculated by Bates & Dalgarno (1953). This factor should actually go into the integrals of the reaction rates $\langle\sigma_x v\rangle_s$ and $\langle\sigma_x v\rangle_f$ for the second and third terms in equation (3). Rewriting the expression with this minor change, one obtains the final relation

$$\frac{I_b}{I_n} = \frac{\epsilon_A\langle\sigma_x v\rangle_s}{\epsilon_B\langle\sigma_i v\rangle_f} + \frac{\langle g_\alpha\sigma_x v\rangle_s}{\epsilon_B\langle\sigma_i v\rangle_f} + \frac{\langle\sigma_x v\rangle_s\langle g_\alpha\sigma_x v\rangle_f}{\epsilon_B(\sigma_i v\rangle_f^2}\,. \qquad (5)$$

Using equation (5), we have calculated how the intensity ratio varies as a function of shock velocity. The details of these calculations are given in the Appendix. Figure 8 shows the relation for both the equilibrated and unequilibrated cases.

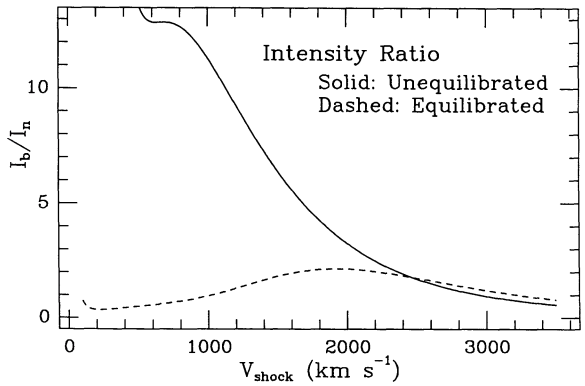

FIG. 8.—The calculated relation between the intensity ratio and the shock velocity. The two curves DO NOT represent the extremes of the theoretical intensity ratio for all shock velocities.

However, these curves do *not* necessarily represent the extremes of the intensity ratio at a given shock velocity due to the complex interplay of all the reaction rates in the formula. Thus, the intensity ratios are not constrained to lie between the curves. The values for the unequilibrated case (the only relation previously calculated) are much larger than those previously reported. This is due for the most part to the calculation of each of the quantities in equation (5), many of which were only approximated in earlier works, and to the use of more recent atomic data.

4. RESULTS AND DISCUSSION

4.1. *Problems with Intensity Ratios*

It is immediately apparent that the calculated intensity ratios bear little resemblance to those observed. In all the SNRs for which the ratio has been measured, no intensity ratio greater than ≈ 1.2 has been seen, with most falling below one. Yet, for the majority of shock velocities, both the unequilibrated and equilibrated models give $I_b/I_n > 1$. We do not believe that the uncertainties in the calculations (either in the atomic data used or in the approximations made) account for the large discrepancies. The most likely explanation seems to lie in the temperature of the electrons. As noted in the previous section, the two curves in Figure 8 do not necessarily represent the extreme values of the intensity ratio. Preliminary calculations indicate that intermediate values of the intensity ratio drop rapidly with equilibration, probably falling below the equilibrated values, and then rise again slowly as the electrons heat up to the ion temperature. We are pursuing these calculations and hope to use this variation, combined with the shock velocity determined from the broad component FWHM, to study the state of equilibration behind this type of shock.

Observationally, measurement of the intensity ratio is plagued by the confusion of sources of narrow Hα emission. An apparent range of shock velocities, as seen in Tycho, is the least troubling, since the observed intensity ratio may be thought of as an average from the region, as long as both the intensity ratio and broad component vary. Narrow Hα emission from regions without detectable broad emission complicates the measurement, as in 0519−69.0, since this narrow Hα contribution to the intensity ratio may be significant. In such cases, while the intensity ratio may represent some average over the shocks present, the observed broad component samples only a subset of the observed shocks. The contribution to Hα emission from radiative shocks might be addressed by subtracting out the narrow Hα from the forbidden-line regions, as determined either from radiative shock models or simply from other radiative shocks. However, for shocks which are truly in transition from collisionless to radiative stages, as suggested for some knots in Kepler's SNR (Blair, Long, & Vancura 1991), such subtraction may not be warranted.

While the width of the broad component is more easily determined from observations and better constrained by theory, it is not a perfect indicator of shock velocities. Projection effects can broaden the line profile if an observation includes shocks at different angles to the line of sight. Also, while all of the calculations make use of Maxwellian velocity distributions, the actual distributions are unknown, since Coulomb interactions have not had time to establish Maxwellian distributions in the postshock regions observed. However, the width of the broad component remains the best method with which to determine the shock velocities.

4.2. *Shock Velocities*

Unlike the intensity ratio, the equilibrated and unequilibrated models for the relation between broad-component FWHM and shock velocity do represent the extremes and therefore provide a good indication of the shock velocity given the observed FWHM. Since there are two sources of uncertainty in the determination of the shock velocity, the fit to the line profile and the equilibration, we quote a range of most probable velocities. The results are summarized in Tables 3A and 3B.

For SN 1006, the observed width of the broad component gives a shock velocity of 2400 km s^{-1} for the unequilibrated extreme and 3240 km s^{-1} for the full equilibration. Taking the fitting uncertainties into account implies a range of shock velocities of 2200–3500 km s^{-1}. SN 1006 is the only remnant of the six observed which shows no variation of line profile along the observed filament, giving the best measurement of the intensity ratio. Although one cannot draw conclusions from the intensity ratio relation in Figure 8, due to the sensitivity to equilibration, it is noteworthy that the observed intensity ratio does fall on the curves for shock velocities of about 3200–3500 km s^{-1}, where the extremes of equilibration give similar intensity ratios.

Our two-dimensional spectrum of Tycho shows large variations in the line profile. Our best estimate of the FWHM of emission from knot "g" yields a shock velocity of 1850 km s^{-1} for the unequilibrated case and 2500 km s^{-1} for the equilibrated case, or a range of shock velocities of 1500–2800 km s^{-1}. With substantial variations in the line profile, and thus shock velocity, Tycho presents the opportunity to establish an observational relation between intensity ratio and the shock velocity. Such a study would require significantly better signal to noise in the faint filaments, both around the knot and elsewhere, than is available in the spectra discussed here.

For the one location in 0548−70.4 where we detected a broad component, we derive a shock velocity of 670 km s^{-1} assuming no equilibration, and $v_s = 890$ km s^{-1} assuming full equilibration. Taking into account the observational uncertainties, we arrive at a range of 500–1100 km s^{-1} for the shock velocity at that position. For the mixture of radiative and Balmer-dominated shocks observed in 0505−67.9, we derive a shock velocity of 480 km s^{-1} for no equilibration or 640 km s^{-1} for full equilibration. This gives a range of probable shock velocities of 300–800 km s^{-1}. Using the Sedov approximation, $t = 2R/5v_s$, both of these remnants are $\sim 10^4$ yr old. Their ages, relatively low shock velocities (compared with the younger SNRs observed), and forbidden-line emission all suggest that these remnants are in transition from Balmer-dominated SNRs to "normal," radiative shock SNRs.

The remnant 0519−69.0, on the other hand, is a more typical Balmer-dominated SNR, with no forbidden-line emission detected and a shock velocity in the range of 1000–1900 km s^{-1} (1180 km s^{-1} unequilibrated, 1580 km s^{-1} equilibrated) at the one location where we detected a broad component. The second slit position of 0519−69.0 shows no evidence of broad Hα, so we can only give a rough lower bound on the shock velocity. Based on the detection threshold discussed in § 2, we could detect shocks with velocities up to $\sim$2000 km s^{-1}. Thus we could neither confirm nor refute the 2900 km s^{-1} shock in 0519−69.0 claimed by Tuohy et al. (1982). Using the shock velocity of about 1000 km s^{-1} we found in one location as a lower limit and 3000 km s^{-1} as an upper limit for the average shock velocity throughout the rim,

TABLE 3A

RESULTS FOR GALACTIC BALMER-DOMINATED SNRs

SNR	SHOCK VELOCITY FROM FWHM OF BROAD COMPONENT: Unequilibrated (km s^{-1})	SHOCK VELOCITY FROM FWHM OF BROAD COMPONENT: Equilibrated (km s^{-1})	PROBABLE RANGE FOR SHOCK VELOCITY (km s^{-1})	PROPER MOTION[a] (arcsec yr^{-1})	DISTANCE (kpc)	DIAMETER (pc)
SN 1006	1850	2500	1500–2800	0.20 ± 0.01	1.5–3.1	3.5–7.7
Tycho	2400	3240	220–3500	0.30 ± 0.04	1.4–2.8	11–26

[a] Proper motion for SN 1006 from Long, Blair, & van den Bergh 1988; that for Tycho from Kamper & van den Bergh 1978.

TABLE 3B

RESULTS FOR BALMER-DOMINATED SNRs IN THE LMC

SNR	SHOCK VELOCITY FROM FWHM OF BROAD COMPONENT: Unequilibrated (km s^{-1})	SHOCK VELOCITY FROM FWHM OF BROAD COMPONENT: Equilibrated (km s^{-1})	PROBABLE RANGE FOR SHOCK VELOCITY (km s^{-1})	PREDICTED PROPER MOTION[a] (arcsec yr^{-1})	DIAMETER[b] (pc)	APPROXIMATE AGE ($t = 2R/5v_s$) (yr)
0505−67.9	480	640	300–800	0.001–0.003	20	$\sim 10^4$
0548−70.4	670	890	500–1100	0.002–0.005	27.5	$\sim 10^4$
0519−69.0	1180	1580	1000–1900	0.004–0.01[c]	7.5	500[d]–1500
0509−67.5	...	...	>2000	>0.008	6.7	≤1000

[a] Assuming a distance of 50 kpc.
[b] From Tuohy et al. 1982.
[c] Upper limit based on Touhy et al.'s 1982 shock velocity of 2900 km s^{-1}.
[d] Lower limit based on Touhy et al.'s 1982 shock velocity of 2900 km s^{-1}.

we derive a Sedov age of between 500 and 1500 yr for this remnant. If we assume that the absence of a broad component in 0509−67.5 indicates an even faster shock, this remnant is probably even younger. This makes these remnants among the youngest in the LMC, having exploded in the same millennium as 0540−69.3 (age ≈ 750 yr; Kirshner et al. 1989) and N132D (age ≈ 1300 yr; Lasker 1980).

4.3. *Proper Motions and Distances*

Using the measured proper motions of the two Galactic remnants and the shock velocities determined above, we can estimate their distances, as done by CKR and KWC. We assume that the observed proper motion of the filaments corresponds to the shock wave traveling through a partially neutral cloud. For Tycho, Kamper & van den Bergh (1978) quote a proper motion of $0\farcs20 \pm 0\farcs01$ yr^{-1}. Combined with our range in shock velocity, this measurement gives a range in distance of 1.5–3.1 kpc (including the uncertainty in the proper motion). This range is consistent with estimates using widely differing methods, such as the estimate of $2.2^{+1.5}_{-0.5}$ kpc made by Albinson et al. (1986), based on an analysis of H I absorption toward the remnant, the estimate by Hamilton, Sarazin, & Szymkowiak (1986a) of 3.0 kpc from models of the X-ray spectrum, and the lower limit of approximately 2 kpc set by Black & Raymond (1984) from a study of interstellar absorption in stars in the direction of Tycho. It also corresponds well with Strom's (1988) estimate of 2.5 kpc based on adiabatic expansion. At this distance, the diameter is 3.6–7.5 pc (using an angular diameter of 8′.3 from Strom 1988), and the average expansion velocity is 4300–8800 km s^{-1}.

Long, Blair, & van den Bergh (1988) recently remeasured the proper motion of the NW filament in SN 1006 (in the same region as our slit position), deducing a motion of $0\farcs30 \pm 0\farcs04$ yr^{-1}. Based on the KWC estimate of the shock velocity, they derived a distance of 1.7–3.1 kpc to the remnant. Using the range of shock velocities determined in this paper, we improve the estimate to 1.4–2.8 kpc. The lower value (corresponding to little or no equilibration) is consistent with other estimates, which range from 1.1 to 1.7 kpc (Strom 1988; Hamilton, Sarazin, & Szymkowiak 1986b; Wu et al. 1983; Vartanian, Lum, & Ku 1985). The angular diameter of 30′.6 (Strom 1988) corresponds to a diameter of 12–25 pc at this distance. These values give an average expansion velocity of between 6000 and 13,000 km s^{-1}. If SN 1006 was a normal Type Ia supernova, the initial expansion velocity of the bulk of the ejecta was unlikely to have been much more than 12,000 km s^{-1}. Assuming a maximum average expansion velocity of 10,000 km s^{-1} (with a current velocity of 2100–3700 km s^{-1}, this would require dramatic deceleration in the very recent past), a more realistic upper limit to the distance to SN 1006 is 2.3 kpc. Working backward, this upper limit might be interpreted as circumstantial evidence for incomplete equilibration behind the shock, since it is the assumption of full equilibration that gives distances larger than 2.5 kpc.

For the LMC remnants, no proper motion measurements have yet been made, but calculations show that these measurements are possible. Using the shock velocities determined from the width of the broad components in these remnants, and taking 50 kpc as the distance of the LMC (Eastman & Kirshner 1989), we have estimated the proper motions expected for these remnants. For the two which show relatively low shock velocities, 0548−70.4 and 0505−67.9, we infer proper motions of between $0\farcs001$ and $0\farcs005$ yr^{-1}, measurement of which would require a lengthy project. But for 0519−69.0, the predicted proper motion is $0\farcs004$–$0\farcs01$ yr^{-1} (the upper limit based on Tuohy et al.'s (1982) value for the shock velocity in this

remnant). With the possibility of 0.″06 FWHM images at Hα from the *Hubble Space Telescope*, this magnitude of proper motion is measurable in a period of years with image cross correlation techniques (Winkler et al. 1988). Similarly, the expansion of 0509−67.5 might be detectable if its shock is as fast as or faster than that observed in 0519−69.0. Combined with further spectroscopic work to better establish the shock velocities, proper motion measurements would give a direct geometric estimate of the distance to the LMC, independent of any current distance estimate.

5. CONCLUDING REMARKS

The results of our analysis of six SNRs are summarized in Tables 3A and 3B. With the combination of spectral and spatial information obtained in Tycho, we find significant variations in the Hα line profile along the filament containing knot "g." Similar variations are proposed to explain the difference between the shock velocity we derive for one location in 0519−69.0 and that derived by Tuohy et al. (1982). Such variations are expected, since they are accompanied by fluctuations in surface brightness and are probably due to density variations in the local ISM. These changes in the line profile from place to place may make it possible to measure many shock velocity–intensity ratio combinations, perhaps making it possible to create an observationally based relation to compare with theory. Kepler's SNR may also offer such an opportunity (see Blair et al. 1991).

The intensity ratios calculated are significantly different from those previously published, in part due to a typographical error in CKR, but in larger part due to our more accurate calculations of the various rate coefficients. For the unequilibrated case, the ratios are much higher than those observed, at least for shock velocities less than ~ 2500 km s^{-1}. This is weak evidence for at least some prompt equilibration behind the shock, as argued by Cargill & Papadopoulos (1988) based on simulations of plasma instabilities behind collisionless shocks. However, the observed intensity ratios do not correspond to the full equilibration curve either. We are pursuing calculations of intermediate equilibration conditions, which may allow us to use the observed intensity ratios to probe the degree of equilibration behind these shocks.

For the four LMC SNRs studied, the derived shock velocities lead to estimates of the ages and proper motions. The estimated proper motions of 0519−69.0 and 0509−67.5 are large enough to expect that observations with the (corrected) *Hubble Space Telescope* could detect them in a few years. Such observations would provide an independent determination of the distance to the LMC. The implied ages of these two remnants increases to 5 (including SN 1987A) the number of remnants in the LMC with estimated ages less than 1500 yr. This result is consistent with the upper limit on the interval between supernovae of 800 ± 200 years given by Hughes, Helfand, & Kahn (1984). The known young remnants in the LMC set a lower limit of 1.0 SNU for the LMC, where 1 SNU is defined, as in Evans, van den Bergh, & McClure (1989), as one supernovae per $10^{10} L_B(\odot)$ per 100 yr. Their statistical estimate of 31 SNU for the rate in irregular galaxies is artificially high due to the occurrence of SN 1987A, but our lower limit is comparable to the rates they quote for late-type spiral galaxies. Human history is short, and the sampling period for supernovae observations is even shorter. SNRs increase the sampling time to tens of thousands of years and can provide important comparisons for the SN rates derived from recent supernovae.

We are grateful to John Raymond for many long discussions on both the physics and interpretation of Balmer-dominated shocks, and to Roger Chevalier for additional help, as well as for pointing out the typographical error in equation (5) in CKR. Thanks also to Jack Hughes and Eric Schlegel for helpful comments on the reduction and analysis of the spectra presented here, and to Martin Laming for helpful discussions and input on the calculations in § 3. This work was supported in part by the National Science Foundation through grants AST 85-16537 and AST 89-55529 to Harvard University and AST 85-20557 to Middlebury College. IRAF is distributed by the National Optical Astronomy Observatories, which is operated by the Associated Universities for Research in Astronomy, Inc. under cooperative agreement with the National Science Foundation.

APPENDIX A

CALCULATION OF THE INTENSITY RATIO

Calculation of the intensity ratio using equation (5) involves computation of the various rate coefficients, none of which have simple analytic solutions. Several assumptions were made to simplify the computation of these integrals. First it was assumed that the gas was pure hydrogen. The major effect of this assumption is to lower the equilibrated ion (proton) temperature, but this makes differences of only 5%–10% in the equilibrated case. The effects on the unequilibrated case should be even smaller, since the protons and electrons are considered completely independent. We also assume that the protons and electrons in the postshock gas were in Maxwellian distributions.

For charge exchange from slow neutrals (those at preshock temperatures) to fast protons (at postshock temperatures), we assume the slow neutrals are stationary, as in CKR, and obtain

$$\langle \sigma_x v \rangle_s = \left(\frac{l}{\pi^{1/2} v_0} \right) \int_0^\infty v^2 \sigma_x(v) \{ \exp\left[-l^2 (v - v_0)^2 \right] - \exp\left[-l^2 (v + v_0)^2 \right] \} dv \, . \tag{A1}$$

In this equation, $l^2 = m_p / 2kT$ and $T = \mu v_0^2 / 3k$. The bulk velocity, v_0, is $\frac{3}{4}$ the shock velocity, m_p is the mass of the proton, and μ is the mean mass per particle. The integral for charge exchange into excited states, $\langle g_\alpha \sigma_x v \rangle_s$, was calculated in a similar fashion. Since the fast protons and fast neutrals are at the same temperature, the reaction rate coefficient for charge exchange from fast neutrals to fast

protons into excited states is

$$\langle g_\alpha \sigma_x v\rangle_f = 4\pi\left(\frac{m_r}{2\pi kT}\right)^{3/2}\int_0^\infty g_\alpha v^3\sigma_x(v)\exp\left(-\frac{m_r v^2}{2kT}\right)dv\,, \tag{A2}$$

where m_r, the reduced mass for this reaction, is simply $\frac{1}{2}m_p$.

The reaction rate coefficient for ionization of fast neutrals, $\langle\sigma_i v\rangle_f$, was calculated similarly. The rate coefficient can be broken down into two integrals, one for ionization by protons and one for ionization by electrons. For the equilibrated case, all the particles are at the same temperature, so that the total rate coefficient is

$$\langle\sigma_i v\rangle_f = 4\pi\left(\frac{m_{rp}}{2\pi kT}\right)^{3/2}\int_0^\infty v^3\sigma_{ip}(v)\exp\left(-\frac{m_{rp}v^2}{4kT}\right)dv + 4\pi\left(\frac{m_{re}}{2\pi kT}\right)^{3/2}\int_0^\infty v^3\sigma_{ie}(v)\exp\left(-\frac{m_{re}v^2}{2kT}\right)dv\,. \tag{A3}$$

In this equation, m_{rp} and m_{re} are the reduced masses for the interactions, $\frac{1}{2}m_p$ and m_e, respectively. The cross section for ionization by protons, σ_{ip}, was calculated from the formula of Janev & Presnyakov (1980), and that for electrons, σ_{ie}, was taken from the fits given by Janev et al. (1987). For the unequilibrated case, the integral for electron ionization cannot be simplified to a single integral, since the electrons and neutrals are at different temperatures. For this case, we made the approximation that there is no ionization by electrons, so that $\langle\sigma_i v\rangle_f$ is simply the first term of equation (A3). This approximation is correct for shock velocities below about 1000 km s^{-1}, since the electrons are not heated above the ionization threshold of hydrogen. Above $v_s = 1000$ km s^{-1}, the approximation breaks down, leading to an underestimate of the ionization by about 25%, which in turn leads to an overestimate of the intensity ratio in this region by about the same amount.

All of the integrals were computed for the unequilibrated and equilibrated cases and for many shock velocities. The results were then combined using equation (5) to form the intensity ratio as a function of shock velocity, as shown in Figure 8.

REFERENCES

Albinson, J. S., Tuffs, R. J., Swinbank, E., & Gull, S. F. 1986, MNRAS, 219, 427
Bates, D. R., & Dalgarno, A. 1953, Proc. Phys. Soc. London A, 66, 972
Black, J. H., & Raymond, J. C. 1984, AJ, 89, 411
Blair, W. P., Long, K. S., & Vancura, O. 1991, ApJ, 366, 184
Cargill, P. J., & Papadopoulos, K. 1988, ApJ, 329, L29
Chevalier, R. A., & Raymond, J. C. 1978, ApJ, 225, L27 (CR)
Chevalier, R. A., Kirshner, R. P., & Raymond, J. C. 1980, ApJ, 235, 186 (CKR)
Dopita, M. A. 1977, ApJS, 33, 437
Eastman, R. G., & Kirshner, R. P. 1989, ApJ, 347, 771
Evans, R., van den Bergh, S., & McClure, R. D. 1989, ApJ, 345, 752
Fesen, R. A., Blair, W. P., & Kirshner, R. P. 1985, ApJ, 292, 29
Fesen, R. A., Becker, R. H., Blair, W. P., & Long, K. S. 1989, ApJ, 338, L13
Freeman, E. L., & Jones, E. M. 1974, Atomic Collision Processes in Plasma Physics Experiments I, UKAEA Report CLM-R137 (Culham Laboratory, Abingdon, England)
Hamilton, A. J. S., Sarazin, C. L., & Szymkowiak, A. E. 1986a, ApJ, 300, 713
———. 1986b, ApJ, 300, 698
Hughes, J. P., Helfand, D. J., & Kahn, S. M. 1984, ApJ, 281, L25
Janev, R. K., & Presnyakov, L. P. 1980, J. Phys, B., 13, 4233
Janev, R. K., Langer, W. D., Evans, K., Jr., & Post, D. E., Jr. 1987, Elementary Processes in Hydrogen-Helium Plasmas (New York: Springer Verlag)
Kamper, K., & van den Bergh, S. 1978, ApJ, 224, 851
Kirshner, R. P., & Chevalier, R. A. 1978, A&A, 67, 267
Kirshner, R. P., Morse, J. A., Winkler, P. F., & Blair, W. P. 1989, ApJ, 342, 260
Kirshner, R. P., Winkler, P. F., & Chevalier, R. A. 1987, ApJ, 315, L135 (KWC)
Lasker, B. M. 1980, ApJ, 237, 765
Long, K. S., & Blair, W. P. 1990, ApJ, 358, L13
Long, K. S., Blair, W. P., Kirshner, R. P., & Winkler, P. F. 1990, ApJS, 72, 61
Long, K. S., Blair, W. P., & van den Bergh, S. 1988, ApJ, 333, 749
Long, K. S., Helfand, D. J., & Grabelsky, D. A. 1981, ApJ, 248, 925
Mathewson, D. S., Ford, V. L., Dopita, M. A., Tuohy, I. R., Long, K. S., & Helfand, D. J. 1983, ApJS, 51, 345
McClure, G. W. 1966, Phys. Rev., 148, 47
McKee, C. F. 1974, ApJ, 188, 335
McKee, C. F., & Hollenbach, D. J. 1980, ARA&A, 18, 219
Minkowski, R. 1959, in IAU Symposium 9, Paris Symposium on Radio Astronomy, ed. R. N. Bracewell (Stanford: Stanford University Press), p. 316
Raymond, J. C. 1979, ApJS, 39, 1
Raymond, J. C., Blair, W. P., Fesen, R. A., & Gull, T. R. 1983, ApJ, 275, 636
Schmidt, G. D., Weymann, R. J., & Foltz, C. B. 1989, PASP, 101, 713
Strom, R. G. 1988, MNRAS, 230, 331
Tuohy, I. R., Dopita, M. A., Mathewson, D. S., Long, K. S., & Helfand, D. J. 1982, ApJ, 261, 473
Vartanian, M. H., Lum, K. S. K., & Ku, W. H. 1985, ApJ, 288, L5
Winkler, P. F., Tuttle, J. H., Kirshner, R. P., & Irwin, M. J. 1988, in Supernova Remnants and the Interstellar Medium, ed. R. S. Roger and T. L. Landecker (Cambridge: Cambridge University Press), p. 65
Wu, C.-C., Leventhal, M., Sarazin, C. L., & Gull, T. R. 1983, ApJ, 269, L5